Unimolecular decomposition of NO_3: The $NO+O_2$ threshold regime

K. Mikhaylichenko, C. Riehn,[a] L. Valachovic, A. Sanov, and C. Wittig
Department of Chemistry, University of Southern California, Los Angeles, California 90089-0482

(Received 13 June 1996; accepted 16 July 1996)

The unimolecular decomposition of expansion-cooled NO_3 has been investigated in the threshold regime of the $NO+O_2$ channel. Photoexcitation in the region 16 780–17 090 cm^{-1} (596–585 nm) prepares ensembles of molecular eigenstates, each of which is a mixture of the $B\ ^2E'$ bright state and lower electronic states. The $X\ ^2A_2'$ ground state is believed to be the probable terminus of $^2E'$ radiationless decay, though participation of $A\ ^2E''$ is also possible. For these photon energies, unimolecular decomposition occurs exclusively via the $NO+O_2$ channel, and NO yield spectra and state distributions have been obtained. The yield spectra are independent of the rotational state monitored, as expected for a large reverse barrier. The state distributions are insensitive to the photolysis photon energy and can be rationalized in terms of dynamical bias. The NO yield goes to zero rapidly above the $O+NO_2$ threshold (17 090±20 cm^{-1}). Because of tunneling, the $NO+O_2$ channel does not have a precise threshold; the value 16 780 cm^{-1} is the smallest photon energy that yielded signals under the present conditions. Very small decomposition rates were obtained via time-domain measurements in which reactive quenching of long-lived NO_3 fluorescence was observed. The rates varied from 1×10^4 at 16 780 cm^{-1} to 6×10^7 s^{-1} at 16 880 cm^{-1}, and their collision free nature was confirmed experimentally. These data were fitted by using a one-dimensional tunneling model for motion along the reaction coordinate combined with the threshold Rice–Ramsperger–Kassel–Marcus (RRKM) rate. The top of the $NO+O_2$ barrier is estimated to lie at 16 900±15 cm^{-1}. Translational energy measurements of specific NO ($X\ ^2\Pi_\Omega, v, J$) levels showed that O_2 is highly excited, with a population inversion extending to energies above the $a\ ^1\Delta_g$ threshold, in agreement with previous work. It is possible that the main O_2 product is $X\ ^3\Sigma_g^-$, though some participation of $a\ ^1\Delta_g$ cannot be ruled out. Within the experimental uncertainty, $b\ ^1\Sigma_g^+$ is not produced. © *1996 American Institute of Physics.* [S0021-9606(96)00240-1]

I. INTRODUCTION

Polyatomic molecules and radicals that exhibit a breakdown of the Born–Oppenheimer approximation and have alternative pathways for unimolecular decay are of great interest in physical chemistry. Detailed studies of such species improve our understanding of how nonadiabatic interactions between zeroth-order electronic potential energy surfaces (PESs) affect the reaction pathways of an excited molecule as it evolves to products. Ultimate goals range from a deeper understanding of the relevant physical and chemical processes to the control of chemical reactivity. In consideration of the above, the nitrate radical (NO_3) provides an excellent model system for examining those aspects of its molecular physics that are involved in chemical change via unimolecular reactions.

Since the discovery of the night-time presence of NO_3 in both the stratosphere[1] and troposphere,[2] NO_3 has been recognized as an important participant in a growing list of atmospherically relevant chemical transformations (e.g., conversion of NO_x to HNO_3; hydrocarbon and halocarbon oxidation). Furthermore, the photolysis of NO_3 at visible wavelengths is known to yield NO, which contributes to the catalytic destruction of ozone.[3] Appreciation of the atmospheric significance of NO_3 has resulted in numerous spectroscopic and kinetics studies;[4] however, its absorption spectrum, electronic states, intramolecular dynamics, and photochemistry are not well understood. The main reason that NO_3 has not been more thoroughly investigated experimentally is the difficulty of preparing sufficiently clean, yet intense, beams of cold NO_3 for studies in collision-free environments.

The only low-lying, optically accessible state of NO_3 is $B\ ^2E'$. Its absorption features lie at convenient photon energies, and the $^2E'\leftarrow{}^2A_2'$ system has a large absorption cross section ($\sigma_{662\ \mathrm{nm}}=2.2\times10^{-17}$ cm^2).[5,6] Fluorescence following excitation in the region of 604–678 nm is characterized by diffuse bands[7,8] and by the Douglas effect.[9] Namely, the fluorescence lifetimes are much longer than the radiative lifetime of the zeroth-order $^2E'$ state (i.e., several hundred microseconds versus ~1 μs, respectively).[10]

The three low-lying doublets (i.e., the $X\ ^2A_2'$ ground state, $A\ ^2E''$ at 7005 cm^{-1}, and $B\ ^2E'$ at 15 110 cm^{-1}) are subject to strong nonadiabatic (vibronic) interactions that mix the zeroth-order electronic states.[11] Consequently, $^2E'$ undergoes internal conversion to a quasicontinuum of near-isoenergetic dark levels, resulting in a dense manifold of molecular eigenstates having mixed $^2E'/{}^2A_2'$ electronic character, with possible contributions from $^2E''$. As a result, although the wave functions of the optically excited radical

[a]Permanent address: Universität Frankfurt a. M., Institut für Physikalische und Theoretische Chemie, Marie-Curie-Str. 11, D-60439 Frankfurt a. M., Germany.

retain some $^2E'$ electronic character, they are dominated by the lower electronic manifolds on time scales exceeding the inverse of the mean level spacing, i.e., after any optically prepared coherences have dephased. Note that there is no reason to assume that all members of the full ensemble of molecular eigenstates acquire the same degree of bright character via vibronic interaction, since the most pronounced effect will be to couple levels within the $^2E'$ bright-state manifold to dark levels of the same vibronic symmetry. Following the example of NO_2,[12] weaker interactions (second-order spin–orbit and orbit–rotation)[13] would be responsible for the couplings between levels having different vibronic symmetries.

The nature of the nonadiabatic interactions in NO_3 has been the subject of a number of experimental[14–17] and theoretical[18] investigations. Briefly, these interactions can be described as: (i) Jahn–Teller (JT) intrastate couplings within the doubly degenerate $^2E'$ and $^2E''$electronic states due to doubly degenerate vibrations of e' symmetry (ν_3 and/or ν_4); (ii) linear interstate pseudo-Jahn–Teller (PJT) interactions between $^2E'$ and $^2A_2'$, due to the ν_3 and/or ν_4 vibrations; (iii) bilinear PJT couplings in $^2E'/^2E''$and $^2E''/^2A_2'$ electronic subsets that symmetrywise require excitation of odd quanta of ν_2 in addition to ν_3 and/or ν_4. Since a separate treatment of all vibronic coupling mechanisms does not describe a given electronic state correctly, NO_3 presents a complicated multimode vibronic coupling problem.[11,18,19]

At energies near the $^2E'$origin, were the nuclear motion to transpire exclusively on the ground PES, it would probably be chaotic.[20] Since NO_3 has six vibrational degrees of freedom and a vibrational density of states of $\sim$100 per cm^{-1},[21] even small coupling matrix elements result in efficient mixing of zeroth-order vibrational levels and are expected to lead to complete intramolecular vibrational redistribution (IVR). Any description of vibronic coupling mechanisms in terms of promoting-mode selection rules can be relevant only at short times, since at longer times the vibrational quantum numbers are destroyed by IVR. Such a hierarchy was suggested as a possible explanation for the structure of the NO_3 laser-induced fluorescence (LIF) spectrum near the $^2E' \leftarrow {}^2A_2'$ origin.[14] Specifically, the width of the LIF spectrum indicates that the zeroth-order $^2E'$ state survives for only $\sim$100 fs, and if this relaxation occurs via levels with promoting-mode character, these levels will decay via IVR into the quasicontinuum of vibrational levels.

Dissociation proceeds via two pathways, with reaction (1) dominating only below the reaction (2) threshold (Fig. 1)

$$NO_3 \rightarrow NO + O_2, \quad \Delta H \approx 1000 \ \ cm^{-1}, \tag{1}$$

$$\rightarrow O + NO_2, \quad \Delta H \approx 17\,000 \ \ cm^{-1}. \tag{2}$$

Geometric properties of the reactant and products are shown in Fig. 2.[17,22,23] Whereas reaction (2) occurs via simple bond fission, reaction (1) involves a three-center mechanism and a tight transition state, i.e., the ground PES correlates to $NO+O_2$ via a barrier along the reaction coordinate. This barrier presumably arises from an avoided crossing of the ground PES with a repulsive PES correlating to $NO+O_2$,

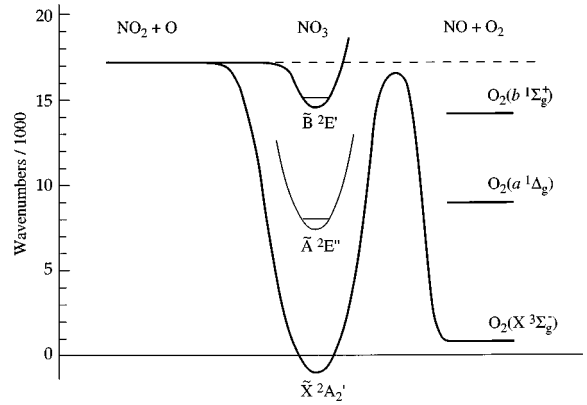

FIG. 1. Energy level diagram showing low-lying NO_3 doublets and energetically accessible O_2 electronic states.

and its presence permits tunneling. In most chemical systems, tunneling of species other than electrons is significant only for hydrogen.[24] An example relevant to the present discussion is HFCO, where the HF+CO channel has been observed as much as 2000 cm^{-1} below the barrier.[25] Though tunneling probabilities are quite small when larger masses are involved, tunneling will nonetheless dominate as long as competitive decay paths such as spontaneous emission and collisional deactivation are relatively slow. In this regard, due to the very small radiative rates of its individual eigenstates, NO_3 is an ideal candidate to observe heavy-particle tunneling under collision-free conditions.

The narrow $NO+O_2$ reaction window has been observed recently by using the molecular beams technique to obtain photofragment translational energy distributions.[26] Since reaction (1) can contribute to the catalytic destruction of ozone,[3] it is important to determine the photon energy range over which it takes place. From the wavelength dependence of the NO time-of-flight (TOF) signal, the reaction (1) barrier was placed at 16 555±280 cm^{-1} and the reaction (2) threshold was found to be 17 040±90 cm^{-1}. A NO_3 rotational temperature of $\sim$70 K precluded a more precise threshold determination. A substantial yield of O_2 ($X\ ^3\Sigma_g^-$)was ob-

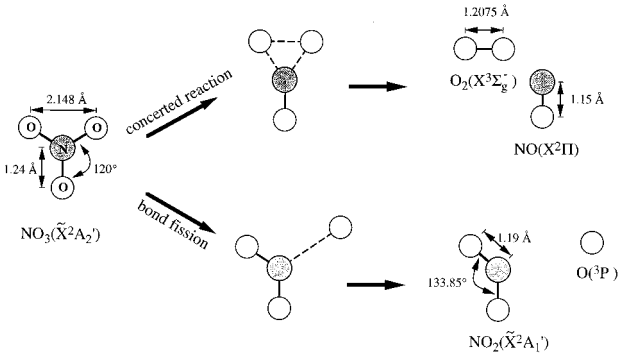

FIG. 2. Schematic diagram showing geometrical properties of NO_3 and reaction products. Molecular parameters are from Ref. 17 (NO_3), Ref. 22 (NO_2), and Ref. 23 (NO and O_2).

served for photolysis below 16 835 cm^{-1}. However, at 17 005 cm^{-1} the O_2 internal energy distribution was seen to peak at ~13 400 cm^{-1}, suggesting the possible participation of the $a\ ^1\Delta_g$ state, which lies 7918 cm^{-1} above the $X\ ^3\Sigma_g^-$ ground state. Unfortunately, the measurements do not distinguish between high vibrational levels of $^3\Sigma_g^-$ and low vibrational levels of $^1\Delta_g$.

As the photon energy is increased above the $O+NO_2$ threshold, k_2 quickly exceeds k_1. The $^2E'$ surface is believed to correlate to ground state $O+NO_2$ via a path without an exit barrier, and it has been suggested that reaction (2) might proceed directly via the $^2E'$ surface following photoexcitation.[10] On the other hand, internal conversion to highly excited vibrational levels of the ground PES can be followed by competition between reactions (1) and (2). Even on the ground PES, k_2 will eventually dominate with increasing energy due to the qualitatively different transition states. Accordingly, the NO yield spectrum just above the reaction (2) threshold will reflect transition state properties as well as the different couplings.

This paper reports an experimental study of NO_3 unimolecular decay. Photoexcitation in the region 16 530–17 240 cm^{-1} (605–580 nm) has been used to record LIF spectra of expansion-cooled NO_3 and to initiate its unimolecular decomposition. Reaction mechanisms have been investigated by recording NO yield spectra and state distributions. In addition, collision-free decomposition rates were recorded both by monitoring the NO yield as the pump–probe delay was varied, as well as by monitoring the quenching of the long-lived NO_3 fluorescence. Rates as low as $1\times10^4\ s^{-1}$ are reported and a tunneling mechanism is implicated. Finally, state-selective center-of-mass (c.m.) translational energy measurements have been used to estimate O_2 internal energy distributions for specific NO ($X\ ^2\Pi_\Omega, v, J$) levels. The distributions peak ~10 000 cm^{-1}, with at least one-third of the population formed in $X\ ^3\Sigma_g^-$ below the $a\ ^1\Delta_g$ threshold. This portion displays a population inversion which is most likely vibrational. Though a significant portion of the population lies above the $a\ ^1\Delta_g$ threshold, the role of $a\ ^1\Delta_g$ versus $X\ ^3\Sigma_g^-$ is unclear; it is possible that $X\ ^3\Sigma_g^-$ dominates.

II. EXPERIMENTAL ARRANGEMENT

An intense beam of cold NO_3 was developed, based on the pulsed pyrolysis of N_2O_5 using a Chen-type nozzle.[27] Ar was bubbled through N_2O_5 cooled to −15 °C (N_2O_5 vapor pressure ~20 Torr; total pressure ~1.1 atm). The resulting 2% N_2O_5/Ar mixture was expanded through a piezoelectrically activated valve (0.5 mm orifice diam) into a resistively heated SiC tube (25 mm×2.2 mm O.D.×1.2 mm I.D.) and then into a low pressure chamber (Fig. 3). Under typical nozzle operating conditions (10 Hz, 500 μs pulse duration) the chamber pressure was $<10^{-4}$ Torr, with a base pressure of $\sim10^{-6}$ Torr. NO_3 production was optimized by adjusting the nozzle temperature while monitoring $^2E'\leftarrow{}^2A_2'$ LIF near 662 nm. The present design allowed us to achieve high NO_3 concentrations in the expansion (despite the concomitant production of NO_2) and good rotational cooling.

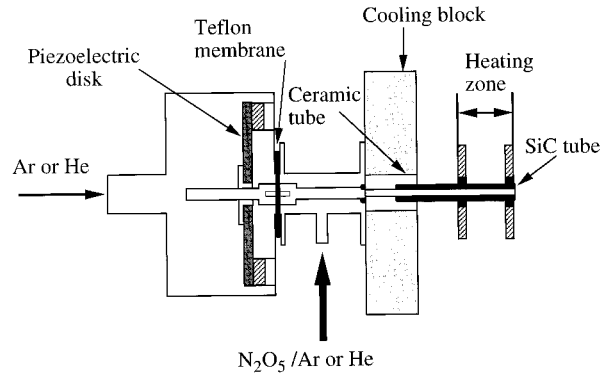

FIG. 3. Schematic diagram of the pulsed pyrolysis nozzle.

Because rotational components of the NO_3 $^2E'\leftarrow{}^2A'$ spectrum are unassigned, T_{rot} was estimated by assuming that cooling is the same as for the coexpanded NO_2. Relative intensities of NO_2 transitions near 16 709 cm^{-1} [$R(0)/R(2)$ and $P(2)/P(4)$][28] were used, and it was found that Ar carrier cools more efficiently than He carrier (6±1 vs 25±1 K).

The LIF apparatus has been described previously.[29] Briefly, a Nd:YAG-pumped dye laser was used to excite NO_3 via the $^2E'\leftarrow{}^2A_2'$ system, and the doubled output of an excimer-pumped dye laser was used for LIF detection of NO via the $A\ ^2\Sigma^+\leftarrow X\ ^2\Pi$ system. The excitation and probe beams were counterpropagated with beam diameters of 2.5 and 1 mm, respectively, in the interaction region. Typical energies were 5–10 mJ for the excitation laser and ~100 μJ for the probe laser.

Since NO_2 has LIF features in the same spectral region as NO_3, a portion of the LIF signal near the opening of the $NO+O_2$ channel is due to the NO_2 that is present in the expansion. For the NO yield measurements, NO_2 fluorescence was eliminated by using an interference filter. Signal due to NO background in the expansion was an order of magnitude smaller than the NO signal arising from NO_3 photodissociation when probing low NO rotational states ($J < 3.5$). For higher NO rotational levels, signals from the NO background were negligible.

In pump–probe experiments, fluorescence was collected perpendicular to the laser/molecular-beam plane with a photomultiplier tube (PMT) which monitored a 3 mm region along the central portion of the expansion. NO yield spectra were recorded for photon energies in the range of 16 780–17 090 cm^{-1} and at various delays between the excitation and probe pulses. NO product state distributions were recorded at a pump–probe delay of 350 ns. The probe energy was sufficient to ensure complete saturation for all rotational branches.

Reaction rates were measured by monitoring their quenching of NO_3 fluorescence in real time. The PMT was placed on the expansion axis 30 cm from the interaction region and fluorescence was collected by the photocathode without the use of imaging optics. Scattered laser light was blocked by a filter and NO_3 emission was monitored at

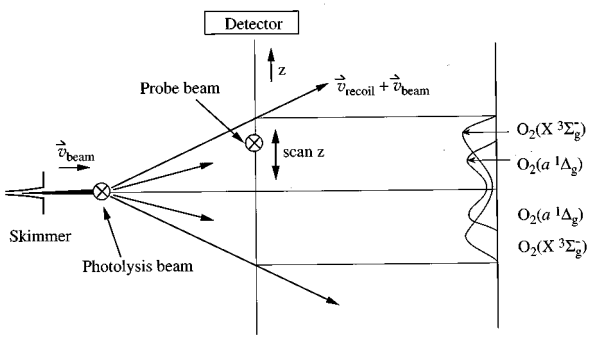

FIG. 4. Schematic diagram of arrangement for correlated NO($^2\Pi_\Omega,v,J$) $+O_2$ distribution measurements. On the right-hand side are examples of the distributions of NO correlated with different O_2 electronic states ($v=0$, $J=0$) assuming a $[X\ ^3\Sigma_g^-]/[a\ ^1\Delta_g]$ ratio of 2.

wavelengths where NO_2 emission is insignificant. This arrangement facilitated monitoring long-lived excited states. The signals reflect both the decay of the excited state and the experimental response function, the latter limiting the estimation of unimolecular decay rates to $\sim 1\times 10^4\ s^{-1}$.

The arrangement for measuring correlated NO $(X\ ^2\Pi_\Omega,v,J)+O_2$ translational energy distributions is shown in Fig. 4; it is the same as that used to study NO_2 unimolecular decomposition.[30] NO_3 is excited in the photolysis region and dissociation takes place as the NO_3 c.m. travels with the molecular beam. After a delay, the products reach the detection region, which is separated spatially from the photolysis region. The NO $(X\ ^2\Pi_\Omega,v,J)$fragments that correlate with different O_2 internal energies reach the probe region spatially separated as per their recoil velocities. By scanning the position of the probe beam in the z direction (Fig. 4), spatial profiles of selected NO($X\ ^2\Pi_\Omega,v,J$) products were obtained at a pump–probe delay of 2.55 μS. To improve resolution, the photolysis and probe beams were focused to diameters of $\sim$0.2 mm in their respective interaction regions. NO was detected by 1+1 REMPI, which provides the highest sensitivity possible.[30] Data analyses take into account: (i) the fact that each NO recoil profile is a sum of contributions from NO fragments correlated with different O_2 states; and (ii) spatial broadening effects due to the finite sizes of the photolysis and probe beams, the v_z velocity components of parent NO_3 in the molecular beam, the NO_3 rotational temperature, and long dissociation times.[30,31]

Spatial anisotropy is not expected because of the small NO_3 dissociation rates. The NO signal is observed at all values of $|z|$ smaller than the appearance threshold defined by the recoil velocity and the pump–probe delay. However, due to the geometrical arrangement, spatial profiles for a given $|z|$have maximum intensity at their furthest displacements from the molecular beam axis, i.e., where the probe beam illuminates the recoil sphere at a grazing angle. This is illustrated by the profiles on the right-hand side of Fig. 4. It is also noted that this arrangement is more sensitive to the slower recoiling products since the two-dimensional number-density of products on the surface of the recoil sphere decreases quadratically with radius, which is proportional to recoil velocity.

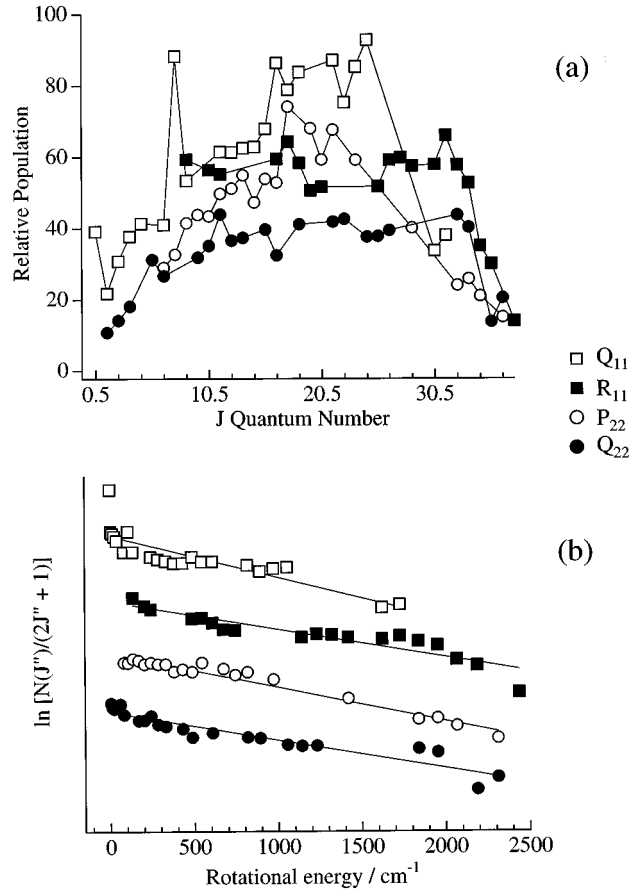

FIG. 5. (a) NO($v=0$) rotational populations for photolysis at 16 990 cm^{-1}; the lines through the data serve to guide the eye. (b) Boltzmann plots for the data in Fig. 5(a); the lines represent linear fits to the data. All slopes correspond to 1400±300 K.

III. RESULTS

Photolysis at 16 990 cm^{-1} yielded the NO $(X\ ^2\Pi_{1/2,3/2},v=0)$ rotational distributions shown in Fig. 5(a). Vibrational excitation (not shown) is modest, with $\leqslant$10% of the NO formed in $v=1$. The $^2\Pi_{1/2}$ lower spin–orbit state is slightly more populated than the $^2\Pi_{3/2}$ upper spin–orbit state, and the $A'\Lambda$-doublet components are slightly more populated than the A'' components. The rotational distributions shown in Fig. 5(a) can be characterized by using the Boltzmann plots shown in Fig. 5(b). The slopes correspond to 1400±300 K. These slopes should be considered figures of merit rather than temperatures, since they apply to a limited range of rotational levels. NO populations at other photon energies in the range of 16 840–17 000 cm^{-1} were examined and no significant differences were noted.

Figure 6 shows the NO($X\ ^2\Pi_{1/2},v=0,J=13.5$) yield spectrum and the NO_3 LIF spectrum recorded just below the $NO+O_2$ barrier. Since some of the features in the latter are due to NO_2 contamination, a NO_2 LIF spectrum is also shown. Both the NO_3 LIF and the NO yield spectra are in

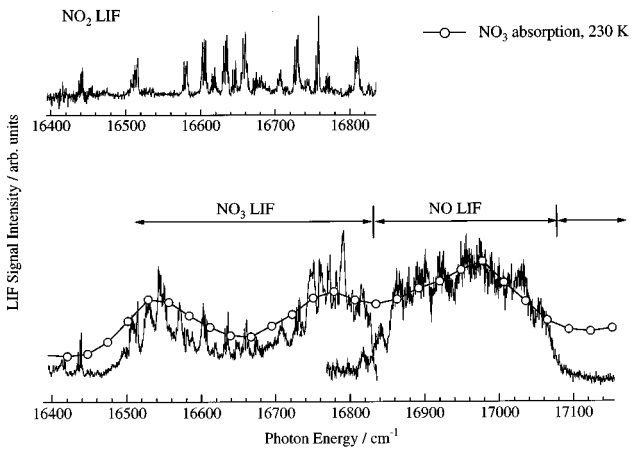

FIG. 6. LIF signals relevant to reaction (1): NO($X\ ^2\Pi_{1/2}$, $v=0$, $J=13.5$) yield spectrum (monitoring R_{11})at a pump–probe delay of 1 μs; NO_3 LIF spectrum just below the $NO+O_2$ barrier (including contaminant NO_2 lines); NO_2 LIF spectrum for T_{rot}=6 K. Also shown (open circles) is the NO_3 230 K absorption spectrum (Ref. 6).

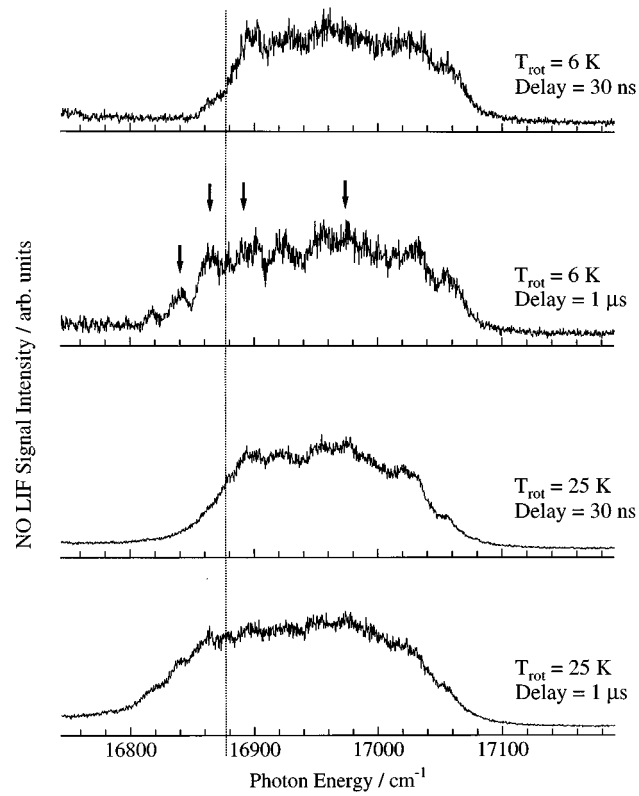

FIG. 7. NO($X\ ^2\Pi_{1/2}$, $v=0$, $J=13.5$)yield spectra at the indicated pump–probe delay times for NO_3 rotational temperatures of 6 and 25 K. Apparent thresholds for T_{rot}=6 and 25 K and 30 ns delay are shown as a vertical dotted line. Arrows indicate the photon energies at which correlated NO ($^2\Pi_\Omega,v,J$)+O_2 distributions were obtained.

accord with the 230 K NO_3 absorption profile.[6] The NO yield spectrum is independent of the rotational state monitored, as expected for a large reverse barrier, and the narrow $NO+O_2$ reaction window is seen to extend from 16 820±40 to 17 090±20 cm^{-1}. As in previous studies,[24] the largest NO signals were recorded near 16 980 cm^{-1}, which corresponds to a peak in the NO_3 absorption.

Below 16 890 cm^{-1}, NO buildup is not prompt on the time scale of the nanosecond-resolution pump–probe measurements. In addition, NO_3 fluorescence is also present in this wavelength region. The existence of a *slow* process associated with reaction (1) is illustrated by the time dependence of the NO yield spectra for rotational temperatures of 6 and 25 K, as shown in Fig. 7. For a pump–probe delay of 30 ns, there is an apparent threshold at 16 878±10 cm^{-1}. However, upon increasing the pump–probe delay, this threshold is shifted to lower energies. For example, for delays as long as ~1 μs, the threshold drops to 16 815 cm^{-1}. For delays longer than ~1 μs, the excited molecules are transported out of the probe region as per the molecular beam velocity. Also, because of the large translational energy release in the exit channel, NO recoil out of the probe region is significant. Thus, monitoring NO buildup times provides an upper limit to the decomposition rates.

The slow unimolecular decay rates described above were also observed via their reactive quenching of the long-lived NO_3 emission. Time resolved emission profiles were obtained at several photon energies, as shown in Fig. 8. Fluorescence quenching was evident above 16 780 cm^{-1} and unimolecular decay rates larger than 1×10^4 s^{-1} could easily be discerned [Fig. 8(c)]. As the photon energy was increased, reactive quenching of the fluorescence increased rapidly [Figs. 8(a) and 8(b)]. At still larger photon energies, measurement of excited state lifetimes was limited by the 30 ns experimental resolution. Since the decay curves contain contributions from both the NO_3 fluorescence and the apparatus response function, the deconvolution of the unimolecular decay rates from the measured traces was done assuming biexponential behavior. Moreover, the fit was sensitive to parameters such as the baseline and zero of time used in the fitting procedure. As a result, the estimated uncertainty for each of the k_1 values is ±50%.

Figure 9 displays k_1 versus photon energy. The rates extracted from the fast components of the decay curves are indicated by open circles and squares. The open circles represent T_{rot}=6 K. These rates increase from 1×10^4 s^{-1} at 16 780 cm^{-1} to 6×10^7 s^{-1} at 16 880 cm^{-1}. The squares represent T_{rot}=20 K (350 Torr nozzle backing pressure, 5 Hz operation). Under these conditions the chamber pressure is $<10^{-5}$ Torr, which is an order of magnitude lower than under the T_{rot}=6 K conditions, thus minimizing beam–gas collisions. The higher value of T_{rot} appears to shift the data to slightly lower photon energies without changing the overall trend. In fact, the shift is comparable to the change in the average parent rotational energies in going from 6 to 20 K. The fact that lowering the backing pressure does not affect the slow reaction is consistent with the collision-free nature of this process.

Spatial distributions of specific NO quantum states were obtained for the photon energies indicated by arrows in Fig. 7. A representative profile obtained at 16 992 cm^{-1} is shown

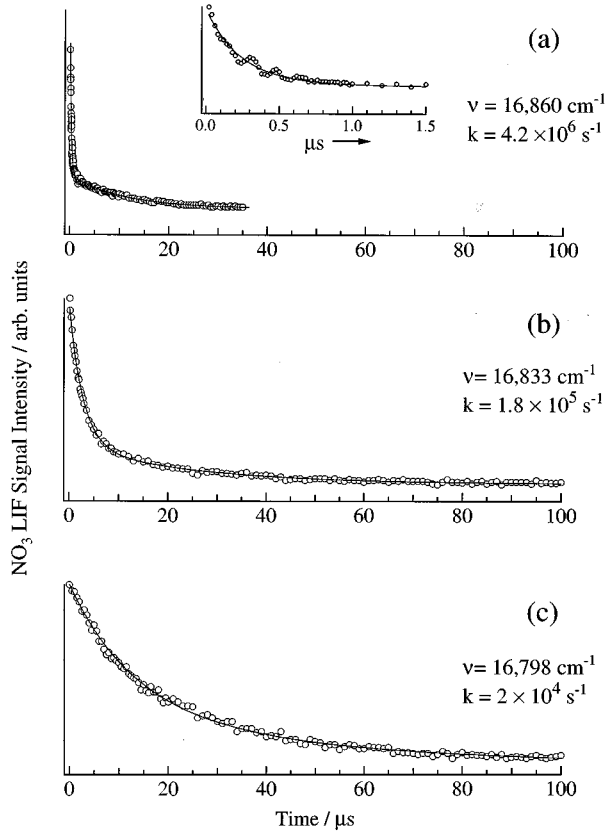

FIG. 8. Time resolved NO_3 emission at the given excitation energies. The lines represent biexponential fits to the data. Also shown are the NO_3 unimolecular decay rates extracted from the fast component of the fluorescence decay curves.

in Fig. 10. The bottom axis indicates the displacement of the monitored NO along the z axis at a pump–probe delay of 2.55 μs. The top axes indicate the appearance thresholds for O_2 electronic and vibrational levels without accounting for

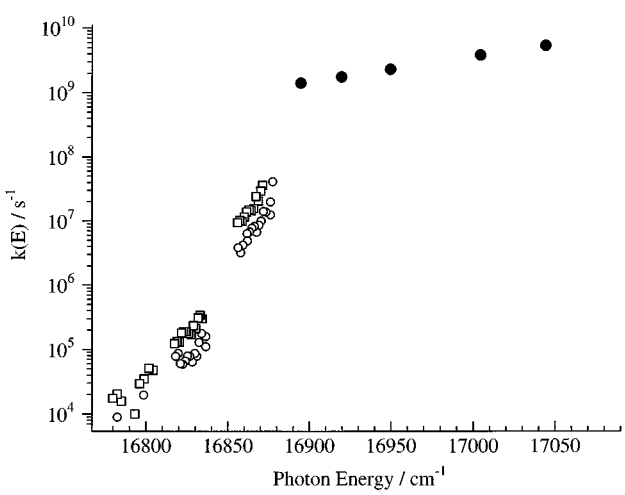

FIG. 9. NO_3 decomposition rate vs photon energy. Open circles and squares represent data obtained by monitoring time resolved NO_3 emission for T_{rot}=6 and ~20 K, respectively. Filled circles represent data obtained by using the picosecond-resolution pump–probe technique averaged over the 60 cm^{-1} linewidth of the ultrafast laser (Ref. 44).

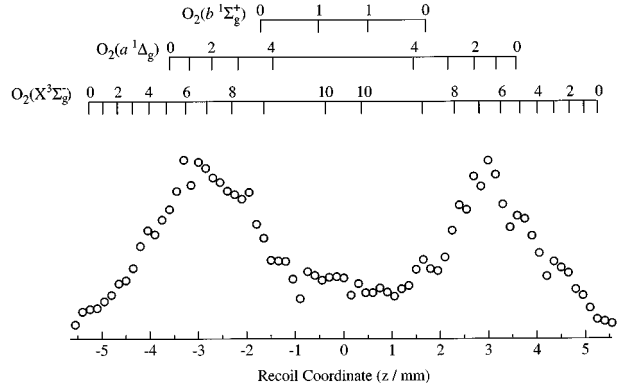

FIG. 10. NO($X\ ^2\Pi_{3/2}$, $v = 0$, $J = 17.5$) spatial profiles obtained at 16 992 cm^{-1} by monitoring the $A\ ^2\Sigma \leftarrow X\ ^2\Pi P_{22}$ transition. The bottom axis gives the distance between the centers of the probe and photolysis beams along the z axis; the top axis lists O_2 internal energies.

experimental broadening. Note that the signal associated with O_2 ($X\ ^3\Sigma_g^-$, $v = 0$)is small. For shorter recoil distances, the signal increases gradually, peaking in the vicinity of the appearance threshold for O_2 internal energies of ~10 000 cm^{-1}. Although this internal energy is sufficient to access the $a\ ^1\Delta_g$ state, no abrupt signal increase is observed near the $a\ ^1\Delta_g$ threshold. In addition, the integrated intensity of the signal arising from NO with enough translational energy to preclude $a\ ^1\Delta_g$ formation accounts for a significant fraction of the total (at least one-third). Thus, the data indicate that $O_2(X\ ^3\Sigma_g^-)$ is formed with a population inversion. Similar results were obtained at 16 863 and 16 892 cm^{-1}, and when monitoring different NO rotational and spin–orbit states.

At 16 841 cm^{-1}, the NO($X\ ^2\Pi_{3/2}$,$v = 0$, $J = 17.5$) spatial profile corresponds to a larger relative population of the lower $O_2(X\ ^3\Sigma_g^-)$levels. However, k_1 is so small (~2×10^5 s^{-1}) that NO buildup is comparable to the maximum pump–probe delay of 3 μs allowed by the dimensions of the apparatus and the product recoil, thus complicating analyses. This preliminary result will be the subject of future work.

IV. DISCUSSION

A. The roles of the $X\ ^2A_2'$, $A\ ^2E''$, and $B\ ^2E'$ states

Nelson *et al.* used the integrated absorption coefficient of the $^2E' \leftarrow {}^2A_2'$ origin to estimate the spontaneous emission lifetime of the zeroth-order $^2E'$ state, obtaining a value of ~1 μs.[10] We confirmed this by using a well-established procedure.[32,33] They also reported long fluorescence lifetimes (τ_{fl}~340 μs) at the $^2E'$ origin (with some evidence for nonexponential decay at shorter times), indicating an oscillator strength dilution factor of ~340 for the observed levels, which span a region of ~50 cm^{-1} around the origin. Thus, in this energy range, ~7 vibronic levels per cm^{-1} (i.e., 340÷50) are mixed with the $^2E'$ bright state, which is considerably less than the estimated density of $^2A_2'$ vibrational levels (~100/cm^{-1}).[34]

On the basis of a dilution factor of ~340, it follows that the $^2E' \leftarrow {}^2A_2'$ oscillator strength is not distributed statisti-

cally among all nearby levels, in which case the dilution factor would be much larger. Such modest dilution can be rationalized if the matrix elements connecting levels of different vibronic symmetries are smaller than typical energy separations between the levels. However, by analogy with NO_2, where second-order spin–orbit and orbit–rotation matrix elements have been found to be several tenths of a wave number,[13] at least *some* coupling between levels of different vibronic symmetries is expected, though oscillator strength may be distributed inhomogeneously among the different vibronic species.

Since it has not been possible to fully quantify the extent of dilution or to establish radiationless decay mechanisms, the relative $^2E''$ and $^2A_2'$ contributions remain unknown. However, $^2E'/^2A_2'$ coupling has been confirmed both experimentally[14–17] and theoretically,[18] and $^2E'/^2E''$ coupling is believed to be a higher-order process.[18,19] Also, $^2A_2'$ is preferred over $^2E''$ on statistical grounds, i.e., at the present energies, the vibrational level density within the $^2A_2'$ manifold is significantly larger than that within the $^2E''$ manifold. Thus, we *assume* that $^2A_2'$ is the main terminus of radiationless decay, though participation of $^2E''$ cannot be ruled out. The conclusions presented below would not be altered seriously by including $^2E''$.

B. Intramolecular dynamics

At the energies and vibrational state densities of interest in the present study, it is highly probable that the nuclear dynamics would be chaotic even if they were to transpire solely on the $^2A_2'$ zeroth-order PES, i.e., ignoring vibronic interactions. This assumption is based on the exhaustive body of experimental and theoretical data that has accrued in the area of intramolecular vibrational dynamics.[20] However, vibronic interactions are known to efficiently promote chaotic dynamics within the vibronic manifolds.[11,35,36] Therefore we assume that the system displays full vibronic chaos for the energies and time scales of interest in the present study, as was found to be the case for NO_2.[12,37] Since couplings between different vibronic species are weaker than the couplings within each vibronic manifold, the system can be vibronically chaotic (i.e., within each manifold) without being rovibronically chaotic (i.e., between manifolds). However, again by invoking analogy with NO_2, where it has been reported that rovibronic chaos exists just below D_0 as a consequence of second-order spin–orbit and orbit–rotation interactions,[13] there exists the possibility that NO_3 is rovibronically chaotic.

C. Optical excitation

The vibronic interactions that mix the zeroth-order electronic states provide a means of optically preparing vibrationally excited states that decay via one or more unimolecular decomposition mechanisms. For example, reaction (1) results from weak couplings between the optically prepared molecular eigenstates[38] and the $NO+O_2$ continuum. From the 50 cm^{-1} width of the $^2E' \leftarrow {}^2A_2'$ origin LIF feature and the dilution of the oscillator strength, it follows that the molecular eigenstates have little $^2E'$ character. Instead, they are dominated by the lower electronic manifolds, tentatively assumed to be $^2A_2'$

$$|\psi_i\rangle = \sum_n \langle {}^2E', v_n|\psi_i\rangle |{}^2E', v_n\rangle + \sum_m \langle {}^2A_2', v_m|\psi_i\rangle |{}^2A_2', v_m\rangle, \tag{3}$$

where $|\psi_i\rangle$ is a molecular eigenstate, the sums over v_n and v_m include all vibrational levels (rotational quantum numbers are suppressed), and $m \gg n$ because of the different vibrational level densities for the $^2E'$ and $^2A_2'$ manifolds. Note that the term ''molecular eigenstate'' is used even when these levels are coupled weakly to a continuum.

For the tunneling regime examined in the present experiments, all of the measured k_1 values are $<10^8$ s^{-1}, which corresponds to Lorentzian widths <0.0005 cm^{-1}. Because of the narrowness of these widths, the energy level structure can be treated as a quasicontinuum of isolated (nonoverlapping) resonances. The high degree of spectral overlap observed experimentally is due to several factors: congestion caused by the many different rotational levels excited when using 6 K samples, the Doppler effect in unskimmed expansions, and the laser linewidth. However, these factors do not lead to quantum interferences, so the approximation of isolated resonances is still valid insofar as the statistical properties of the decay widths is concerned.

Though the decay widths of individual resonances fluctuate about a mean value,[39] the present conditions ensure that a large number of resonances are excited by the laser pulse. Thus, fluctuations between measured k_1 values were neither anticipated nor observed. Moreover, coherences imparted by the photoexcitation step dissipate quickly on the time scale of the rate measurements. Thus, we believe that the excited ensemble of levels can be modeled as decaying incoherently with a distribution of rates. It is the relaxation of this optically prepared ensemble that we record as k_1. The unimolecular decomposition was taken to be single exponential because, within the present experimental uncertainty, it fits. However, there is no theoretical basis for this, and higher quality data may reveal deviations from single-exponential decay.

Photoexcitation does not access the full manifold of molecular eigenstates equivalently. In the absence of saturation, it excites levels in proportion to the squares of their electric dipole matrix elements, and is thus biased. Nonetheless, it is expected that *measured* $k_1(E)$ values differ little from $k_1(E)$ values averaged over *all* molecular eigenstates within the same energy window. The reason is that the reaction rates are not characteristic of the $^2E'$ surface, which carries the oscillator strength but is unreactive toward $NO+O_2$.[10] Since the $^2E'$ surface contributes little to the makeup of individual eigenstates, as seen by its small weighting coefficient in the expansion of the wave function, the distribution of decay rates is expected to be almost independent of the bright-state contribution to the molecular eigenstate.

D. Reaction rates

It follows from the above arguments that reaction (1) can be described as proceeding via the ground PES and that statistical rate models can be applied which: (i) are semiclassical in nature [e.g., RRKM, phase space theory (PST), statistical adiabatic channel model (SACM)] when the resonances are averaged over;[40–42] and (ii) exhibit distributions of decay rates, level spacings, absorption strengths, etc., when the resonances are resolved.[39,43] This picture can be comprised when reactions (1) and (2) compete, specifically, when the latter occurs so rapidly that decay to and within the lower electronic manifolds is incomplete on the time scale of that reaction.

As indicated in Fig. 9, there is no precise reaction (1) threshold—nor, because of the inevitable participation of tunneling, can there be one. The marked variation of k_1 with photon energy shown in Fig. 9 has been verified by repeated measurements and by using two complementary experimental techniques. Namely, rates obtained by monitoring reactive quenching of the NO_3 fluorescence are consistent with rates obtained by recording NO buildup times, though the latter are limited to values $\geqslant 10^6$ s^{-1}. Also, the *collision-free* nature of this slow unimolecular process was confirmed experimentally.

NO_3 decay rates above the reaction (1) barrier have been reported by Davis *et al.*,[44] who used the picosecond-resolution pump–probe technique to record NO buildup times. They found that in the $\sim$200 cm^{-1} window between the top of the barrier and the $O+NO_2$ threshold, k_1 varied from 1 to 5×10^9 s^{-1}, with each measurement averaging rates over the broad (60 cm^{-1}) linewidth of the photolysis laser. These data were fitted by using RRKM theory with a lowest transition state frequency of 70 cm^{-1}.

Figure 9 shows that below the barrier, k_1 varies *much* more rapidly than it does above the barrier, changing by three orders of magnitude in $\sim$100 cm^{-1}. Since small tunneling probabilities display near-exponential dependencies on the area beneath the top of the barrier, such rapid variation is expected. Moreover, tunneling can account for the very different slopes that characterize the regimes above and below $\sim 10^9$ s^{-1} (Fig. 9).[26]

The simplest way to incorporate tunneling into the statistical model is via motion along a one-dimensional reaction coordinate that is separable at the transition state from the orthogonal degrees of freedom. The tunneling probability can then be calculated by using the WKB approximation,[45,46] with the potential along the reaction coordinate taken as an inverted parabola. The resulting expression is[46]

$$P(E')=\frac{\exp(-2\pi E'/\omega_b)}{1+\exp(-2\pi E'/\omega_b)}, \tag{4}$$

where ω_b is the magnitude of the imaginary frequency of the barrier and E' is the energy in the reaction coordinate *below* the zero point of the transition state (i.e., $E'>0$). To obtain ω_b, it is necessary to have the barrier width and the effective mass, parameters which are not known. However, we note that a value of $\omega_b=300$ cm^{-1} (corresponding to a $\sim$1 Å width 100 cm^{-1} below the top of the barrier and an 8 amu effective mass) yields rates that are consistent with the data shown in Fig. 9.

As mentioned above, the NO yield spectrum near the reaction (2) threshold reflects the k_1/k_2 ratio. Whereas reaction (1) proceeds via the $^2A_2'$ ground state, the $^2A_2'$ and $^2E'$ surfaces can both contribute to reaction (2). It is also possible that $^2E''$ participates. It is a daunting task to establish the respective roles of the different PESs involved in reaction (2).

An important point can be made concerning the possible role of $^2E'$; namely, were a unimolecular reaction to proceed exclusively on the zeroth-order $^2E'$ surface, its threshold rate would be $(h\rho)^{-1}\sim10^{12}$ s^{-1}, as estimated by using the ρ value of 0.03/cm^{-1} obtained by direct count.[47] This is too slow to overcome internal conversion, which occurs with a rate of $\sim10^{13}$ s^{-1}, as estimated from the width of the $^2E'$ original LIF feature. Moreover, for reaction rates $>10^{12}$ s^{-1}, the transition state will tighten with increasing energy, preventing the rate from rising as rapidly with energy as predicted by a very loose transition state. Thus, it seems unlikely that unimolecular reaction exclusively via the $^2E'$ surface can dominate in the k_2 threshold region.

Another extreme case is when reactions (1) and (2) both proceed via the ground state surface. This would occur in the event that internal conversion went to completion prior to reaction. In the rate equation limit, the NO yield above the reaction (2) threshold is then determined by the k_1/k_2 ratio, with each of the rates given by

$$k=\frac{N^{\ddagger}(E-E_0)}{h\rho(E)}, \tag{5}$$

where $N^{\ddagger}(E-E_0)$ is the number of open channels at the transition state and $\rho(E)$ is the parent density of states. For a common intermediate, $\rho(E)$ is the same for both decomposition paths, and therefore k_1/k_2 is the ratio of the numbers of open channels at the transition states for reactions (1) and (2), respectively. Since the reaction (1) transition state is tight, its levels can be described as vibrational. Though the frequencies are uncertain, values of 70 and 140 cm^{-1} for the two lowest transition state frequencies yielded $k_1(E)$ values in agreement with the experimental results.[44] This predicts an increase in k_1 by a factor of several within a 100 cm^{-1} energy interval near the $O+NO_2$ threshold. On the other hand, since the reaction (2) transition state is loose, k_2 will increase rapidly with energy relative to k_1, leading to the rapid dominance of reaction (2).

At this point, we have not been able to draw firm conclusions concerning the roles of the zeroth-order PESs insofar as reaction (2) is concerned. An obvious extension of the present work is double-resonance experiments in which the reaction (2) threshold regime is examined with good energy resolution and dissociation via the ground PES is decoupled from the radiationless decay step.

E. NO product state distributions and yield spectra

The NO product state distributions can be rationalized by invoking dynamical bias, namely, since the $NO+O_2$ reverse barrier is large, product excitations are strongly influenced by the transition state region and the exit channel. As anticipated for a large reverse barrier, the NO excitations are insensitive to the photolysis photon energy in the small energy range between the top of barrier and the reaction (2) threshold. The absence of a significant NO ($v \geqslant 1$) population can be understood as vibrational adiabaticity from the transition state to products. Specifically, vibrational quantum numbers in degrees of freedom orthogonal to the reaction coordinate are conserved past the transition state and appear in the fragments. The predominance of NO ($v=0$) suggests that the N–O bond lengths do not differ significantly between the transition state region and free NO. It is also consistent with the stiffness of the N–O stretch coordinate in the exit channel.

The present work provides characterization of the threshold regions of reactions (1) and (2). Much of this information is obtained from NO yield spectra (Fig. 8), whose spectral density is nearly continuous, albeit with a lumpiness that resembles the NO_3 LIF spectra but with poorer resolution.[14] The NO yield spectrum on the low energy side reflects the threshold region of reaction (1), which proceeds *through* the barrier at the lowest energies. On the high energy side, the yield spectrum reflects competition between reactions (1) and (2).

F. Internal excitations

The data shown in Fig. 10 provide qualitative information concerning O_2 internal excitations despite the low resolution. First, the amount of signal associated with O_2 internal energies lying below the $a\ ^1\Delta_g$ threshold is significant. This can only derive from $X\ ^2\Sigma_g^-$ rovibrational excitation. Recall that correcting the raw data shown in Fig. 10 for the R^2 factor (where R is the radius of the recoil sphere) only *enhances* the large-z contribution.[30,31] Thus, $X\ ^3\Sigma_g^-$ is definitely produced as a counterfragment of the monitored NO level. The monotonic increase of the signal up to the $a\ ^1\Delta_g$ threshold indicates a considerable population inversion within the $X\ ^3\Sigma_g^-$ ground electronic state.

In the region where $X\ ^3\Sigma_g^-$ and $a\ ^1\Delta_g$ are both energetically accessible, their separate contributions cannot be resolved. However, the decrease in signal in the spatial region close to the center of the recoil sphere (i.e., where $b\ ^1\Sigma_g^+$ would appear) is clear. Combined with the fact that the experimental method is most sensitive to slow fragments, this observation rules out significant population of the $b\ ^1\Sigma_g^+$ state.

Smith *et al.*[48] have shown that the $O+NO_2 \rightarrow O_2+NO$ bimolecular reaction (300 K) yields O_2 ($X\ ^3\Sigma_g^-$) in high vibrational levels. They report a monotonic decrease in population from $v=6$ to $v=11$, i.e., for O_2 internal energies above 9800 cm^{-1}. Lower vibrational levels could not be detected by using the LIF method they employed, and it was not possible to isolate the respective roles of direct reaction versus reaction via the $NO_3^\dagger$ intermediate. Since $O+NO_2$ collisions can form $NO_3^\dagger$ efficiently, there is the possibility that the observed $X\ ^3\Sigma_g^-$ vibrational levels derive, at least in part, from NO_3 unimolecular decomposition.

The data shown in Fig. 10 indicate a monotonically decreasing population for O_2 internal energies above $\sim$10 500 cm^{-1}. This corresponds to $X\ ^3\Sigma_g^-$ vibrations from $v=6$ or 7 to $v=11$, though, as stated above, neither our measurements nor those of Davis *et al.*[24] resolve the separate contributions from $X\ ^3\Sigma_g^-$ and $a\ ^1\Delta_g$. The data of Davis *et al.* are of superior resolution, showing some vibrational structure, whereas the present results are product state selective. However, the two data sets are consistent and the correspondence between the translational energy distributions and the $X\ ^3\Sigma_g^-$ LIF measurements is striking. We interpret this as supporting a major, if not dominant, role for the $X\ ^3\Sigma_g^-$ state.

If the O_2 internal excitation resides predominantly in $X\ ^3\Sigma_g^-$, there is probably a significant *vibrational* population inversion, since it is unlikely that rotations would be excited to such a large extent. This can be rationalized by a reaction (1) transition state having a long O–O bond relative to free O_2. However, though we would have no difficulty *accepting* a $X\ ^3\Sigma_g^-$ vibrational distribution peaked near $v=6$ or 7 based on this mechanism, there currently exists no basis for independent support, for example, through theoretical calculations.

V. CONCLUSIONS

This paper reports and discusses measurements of NO_3 unimolecular reactions under collision-free conditions. A number of complementary data are presented: NO product yield spectra; NO_3 LIF spectra; NO rotational and fine-structure state distributions; rates of NO_3 decomposition; and O_2 internal energies correlated with a specific NO ($X\ ^2\Pi_\Omega, v, J$) state. The NO_3 intramolecular dynamics are strongly influenced by nonadiabatic interactions in the $B\ ^2E'/A\ ^2E''/X\ ^2A_2'$ electronic subset.[14] Nuclear motions at these energies are believed to be chaotic, resulting in decomposition rates that can be calculated by using statistical theories.

The $NO+O_2$ channel involves molecular eigenstates having modest $^2E'$ character, and dominant character of lower electronic manifolds. The most probable terminus of radiationless decay is believed to be $^2A_2'$, but we leave open the possibility of $^2E''$ participation.

A narrow window exists for the $NO+O_2$ channel. Very slow rates were observed after excitation with photons that promote the system to energies that lie *below* the reaction (1) barrier. Specifically, rates for collision-free photoinitiated unimolecular decomposition ranged from 1×10^4 s^{-1} at 16 780 cm^{-1} to 6×10^7 s^{-1} at 16 880 cm^{-1}. Tunneling is believed to be responsible for this behavior. A simple extension of RRKM theory confirms that tunneling could indeed result in unimolecular decay rates that vary rapidly enough with energy to be consistent with the experimentally measured rates.

NO rotational excitation is modest and the distributions are insensitive to the excitation photon energy. Vibrational excitation is also modest: $[v=1]/[v=0] \sim 0.1$. There is a high degree of O_2 internal excitation, with the $X\ ^3\Sigma_g^-$ ground state produced throughout the entire photolysis region, in agreement with results from previous measurements of c.m. translational energy distributions.[24] A significant fraction (at least one-third) of the O_2 is formed with internal energies below the $a\ ^1\Delta_g$ threshold, and it is assumed that excitation within $X\ ^3\Sigma_g^-$ is predominantly vibrational as opposed to rotational. The distribution within $X\ ^3\Sigma_g^-$ indicates a population inversion which can be rationalized as due to the geometry of the 3-center transition state.

If $O_2(a\ ^1\Delta_g)$ is *not* produced, the most populous $X\ ^3\Sigma_g^-$ vibrational levels are $\sim v=6$ or 7 for the photolysis region 16 860–17 080 cm^{-1}. It is important to keep in mind that the measurements do not distinguish between low-lying vibrational levels within $a\ ^1\Delta_g$ and high vibrational levels of $X\ ^3\Sigma_g^-$. Nonetheless, there is a good possibility that $X\ ^3\Sigma_g^-$ is the dominant O_2 species. For example, Smith *et al.*[48] report that O_2 from the $O+NO_2 \rightarrow NO+O_2$ reaction is formed in vibrational levels whose populations decrease monotonically from $v=6$ to $v=11$. The O_2 internal energy distribution (see Fig. 10) also decreases monotonically over this range, further supporting $O_2(X\ ^3\Sigma_g^-)$ as a major (if not dominant) O_2 species.

Above the $O+NO_2$ threshold, reaction (2) dominates. Though $^2E'$ is believed to correlate without a barrier to ground state products, unimolecular reaction exclusively on $^2E'$ is not fast enough to bypass internal conversion. Specifically, the estimated k_2 value is an order of magnitude smaller than the radiationless decay rate of $10^{13}\ s^{-1}$ inferred from the LIF spectrum of the $^2E' \leftarrow {}^2A_2'$ origin. Therefore, several surfaces may contribute. It is a daunting task to establish the respective roles of the different PESs involved in reaction (2).

ACKNOWLEDGMENTS

We thank D. Arnold, P. Ionov, I. Bezel, H. Reisler, I. W. M. Smith, and F. Davis for valuable input.

[1] J. F. Noxon, R. B. Norton, and W. R. Henderson, Geophys. Res. Lett. **5**, 675 (1978).
[2] U. Platt, D. Perner, A. M. Winer, G. W. Harris, and J. N. Pitts, Jr., Geophys. Res. Lett. **7**, 89 (1980).
[3] R. A. Graham and H. S. Johnston, J. Phys. Chem. **82**, 254 (1978).
[4] R. P. Wayne *et al.*, in *The Nitrate Radical: Physics, Chemistry, and the Atmosphere*, Atmospheric Environment Vol. 25A, edited by R. P. Wayne (Pergamon, Oxford, 1991), pp. 1–206.
[5] S. P. Sander, J. Phys. Chem. **90**, 4135 (1986).
[6] R. J. Yokelson, J. B. Burkholder, R. W. Fox, R. K. Talukdar, and A. R. Ravishankara, J. Phys. Chem. **98**, 13144 (1994).
[7] H. H. Nelson, L. Pasternack, and J. R. McDonald, J. Phys. Chem. **87**, 1286 (1983).
[8] B. Kim, P. L. Hunter, and H. S. Johnston, J. Chem. Phys. **96**, 4057 (1992).
[9] A. E. Douglas, J. Chem. Phys. **45**, 1007 (1996).
[10] H. H. Nelson, L. Pasternack, and J. R. McDonald, J. Chem. Phys. **79**, 4279 (1983).
[11] H. Köppel, W. Domcke, and L. S. Cederbaum, Adv. Chem. Phys. **57**, 59 (1984).
[12] A. Delon, R. Georges, and R. Jost, J. Chem. Phys. **103**, 7740 (1995).
[13] A. Delon, P. Dupré, and R. Jost, J. Chem. Phys. **99**, 9482 (1993).
[14] L. Valachovic, C. Riehn, K. Mikhaylichenko, and C. Wittig, Chem. Phys. Lett. (in press).
[15] A. Weaver, D. W. Arnold, S. E. Bradforth, and D. M. Neumark, J. Chem. Phys. **94**, 1740 (1991).
[16] E. Hirota, K. Kawaguchi, T. Ishiwata, and I. Tanaka, J. Chem. Phys. **95**, 771 (1991); T. Ishiwata, I. Tanaka, K. Kawaguchi, and E. Hirota, *ibid.* **82**, 2196 (1985).
[17] K. Kawaguchi, E. Hirota, T. Ishiwata, and I. Tanaka, J. Chem. Phys. **93**, 951 (1990).
[18] M. Mayer, L. S. Cederbaum, and H. Köppel, J. Chem. Phys. **100**, 899 (1994).
[19] E. Haller, H. Köppel, and L. S. Cederbaum, J. Chem. Phys. **78**, 1359 (1983).
[20] See, for example, D. W. Noid, M. L. Koszykowski, and R. A. Marcus, Annu. Rev. Phys. Chem. **32**, 267 (1981); E. B. Stechel and E. J. Heller, *ibid.* **35**, 563 (1984); V. E. Bondybey, *ibid.* **35**, 591 (1984).
[21] The density of vibrational states in the ground PES near the $^2E'$ origin was obtained by direct harmonic count using the ground state vibrational frequencies from Ref. 8.
[22] G. Herzberg, *Molecular Spectra and Molecular Structure. III. Electronic Spectra and Electronic Structure of Polyatomic Molecules* (Krieger, Malabar, 1991).
[23] K. P. Huber and G. Herzberg, *Molecular Spectra and Molecular Structure. IV. Constants of Diatomic Molecules* (Van Nostrand Reinhold, New York, 1979).
[24] W. H. Miller, Chem. Rev. **87**, 19 (1987).
[25] Y. S. Choi and C. B. Moore, J. Chem. Phys. **97**, 1010 (1992).
[26] H. F. Davis, B. Kim, H. S. Johnson, and Y. T. Lee, J. Phys. Chem. **97**, 2172 (1993).
[27] D. W. Kohn, H. Clauberg, and P. Chen, Rev. Sci. Instrum. **63**, 4003 (1992).
[28] R. E. Smalley, L. Wharton, and D. H. Levy, J. Chem. Phys. **63**, 4977 (1975).
[29] E. Böhmer, S. K. Shin, Y. Chen, and C. Wittig, J. Chem. Phys. **97**, 2536 (1992).
[30] A. Sanov, C. R. Bieler, and H. Reisler, J. Phys. Chem. **99**, 13637 (1995).
[31] H. Ni, J. M. Serafin, and J. J. Valentini, J. Chem. Phys. **104**, 2259 (1996).
[32] R. C. Hilborn, Am. J. Phys. **50**, 982 (1982).
[33] H. Okabe, *Photochemistry of Small Molecules* (Wiley-Interscience, New York, 1978).
[34] A number of vibronic level densities have potential relevance for the $^2E' \leftarrow {}^2A_2'$ origin region. First, consider all levels of E' vibronic symmetry having one quantum of ν_3 or ν_4 excitation. In this case, $\rho \sim 5/cm^{-1}$. According to PJT selection rules, these should have the largest coupling matrix elements with the $^2E'$ bright state. Alternatively, counting *all* levels having E' vibronic symmetry yields $\rho \sim 20/cm^{-1}$, which can be compared to $\rho \sim 100/cm^{-1}$ for all levels within the $^2A_2'$ electronic state irrespective of vibronic symmetry. The similarity between the density of PJT-promoting-mode levels and the density of mixed levels estimated from the oscillator strength dilution factor is noteworthy. However, this may be fortuitous. For example, since measurements of τ_{fl} values in excess of 100 μs are difficult, it is possible that the zero-pressure lifetimes extend even to the millisecond regime.
[35] I. B. Bersuker and V. Z. Polinger, *Vibronic Interactions in Molecules and Crystals* (Springer-Verlag, New York, 1989).
[36] T. A. Brody, J. Flores, J. B. French, P. A. Mello, A. Pandey, and S. S. M. Wong, Rev. Mod. Phys. **53**, 385 (1981).
[37] R. Georges, A. Delon, and R. Jost, J. Chem. Phys. **103**, 1732 (1995).
[38] Each of the optically prepared molecular eigenstates contains a large percentage of ground electronic state character as per the oscillator strength dilution factor.
[39] See, for example, V. I. Kukulin, K. M. Krasnopolsky, and J. Horácek, *Theory of Resonances: Principals and Applications* (Kluwer, Dordrecht, 1989); J. A. Beswick and J. Jortner, Adv. Chem. Phys. **47**, 363 (1981).
[40] P. J. Robinson and K. A. Holbrook, *Unimolecular Reactions* (Wiley, New York, 1972).
[41] W. Forst, *Theory of Unimolecular Reactions* (Academic, New York, 1973).
[42] W. H. Green, C. B. Moore, and W. F. Polik, Annu. Rev. Phys. Chem. **43**, 591 (1992).

[43] W. F. Polik, C. B. Moore, and W. H. Miller, J. Chem. Phys. **89**,3584 (1988); W. F. Polik, D. R. Guyer, C. B. Moore, and W. H.Miller, *ibid*. **92**, 3471 (1990); W. H. Miller, R. Hernandez, andC. B. Moore, *ibid*. **93**, 5657 (1990); R. Hernandez, W. H. Miller, C. B. Moore, and W. F. Polik, *ibid*. **99**, 950 (1993).
[44] H. F. Davis, P. I. Ionov, S. I. Ionov, and C. Wittig, Chem. Phys. Lett. **215**, 214 (1993).
[45] L. D. Landau and E. M. Lifshitz, *Quantum Mechanics* (Pergamon, London, 1958).
[46] W. H. Miller, J. Am. Chem. Soc. **101**, 6810 (1979).
[47] The following $^2E'$ vibrational frequencies were used in calculating densities of states for the 1900–2100 cm^{-1} interval above the $^2E'$ origin: ν_1=773 cm^{-1}, ν_2=944 cm^{-1}, ν_3=1446 cm^{-1} (Ref. 8), and ν_4=380 cm^{-1}.
[48] I. W. M. Smith, R. P. Tuckett, and C. J. Whitham, Chem. Phys. Lett. **200**, 615 (1992).